nature materials

LETTERS

PUBLISHED ONLINE: 25 JANUARY 2016 | DOI: 10.1038/NMAT4544

Biomimetic 4D printing

A. Sydney Gladman[1,2†], Elisabetta A. Matsumoto[1,2†], Ralph G. Nuzzo[3], L. Mahadevan[1,2,4*] and Jennifer A. Lewis[1,2*]

Shape-morphing systems can be found in many areas, including smart textiles[1], autonomous robotics[2], biomedical devices[3], drug delivery[4] and tissue engineering[5]. The natural analogues of such systems are exemplified by nastic plant motions, where a variety of organs such as tendrils, bracts, leaves and flowers respond to environmental stimuli (such as humidity, light or touch) by varying internal turgor, which leads to dynamic conformations governed by the tissue composition and microstructural anisotropy of cell walls[6–10]. Inspired by these botanical systems, we printed composite hydrogel architectures that are encoded with localized, anisotropic swelling behaviour controlled by the alignment of cellulose fibrils along prescribed four-dimensional printing pathways. When combined with a minimal theoretical framework that allows us to solve the inverse problem of designing the alignment patterns for prescribed target shapes, we can programmably fabricate plant-inspired architectures that change shape on immersion in water, yielding complex three-dimensional morphologies.

Plants exhibit hydration-trigged changes in their morphology due to differences in local swelling behaviour that arise from the directional orientation of stiff cellulose fibrils within plant cell walls[6–10]. Emerging pathways for mimicking these dynamic architectures incorporate materials that can respond to external stimuli, such as shape memory alloys[11,12] and swellable hydrogel composites[13,14], and are assembled by methods such as four-dimensional (4D) printing[11,15] and self-folding origami[16–18]. For example, recent efforts to create plant-inspired, shape-changing structures[10] have employed differential swelling in isotropic or composite bilayers and hinges[8,13,14,16]. However, none of these approaches enable shape change using a single material patterned in a one-step process, nor do they utilize a predictive model capable of tackling both the forward and inverse design problems (Supplementary Text and Supplementary Figs 1 and 2). Here, we develop a biomimetic hydrogel composite that can be 4D printed into programmable bilayer architectures patterned in space and time, which are encoded with localized swelling anisotropy that induces complex shape changes on immersion in water.

Our hydrogel composite ink is composed of stiff cellulose fibrils embedded in a soft acrylamide matrix, which mimics the composition of plant cell walls. The composite architectures are printed using a viscoelastic ink that contains an aqueous solution of *N*,*N*-dimethylacrylamide (or *N*-isopropylacrylamide for reversible systems), photoinitiator, nanoclay, glucose oxidase, glucose, and nanofibrillated cellulose (NFC). The constituents serve different purposes: the clay particles are a rheological aid, inducing the desired viscoelastic behaviour required for direct ink writing[19] (Supplementary Fig. 3); glucose oxidase and glucose minimize oxygen inhibition during the ultraviolet curing process by scavenging ambient oxygen[20], thereby improving polymerization in the printed filamentary features (~100 μm to 1 mm in diameter) to yield mechanically robust structures; the wood-derived cellulose fibrils, which bundle into microfibrils with high aspect ratio (~100), serve as stiff fillers ($E > 100$ GPa; ref. 21). After printing under ambient conditions, the acrylamide monomer is photopolymerized and physically crosslinked by the nanoclay particles, producing a biocompatible hydrogel matrix that swells readily in water[22]. (See Methods for further details.)

The efficacy of our biomimetic 4D printing (bio-4DP) method relies on the ability to deterministically define the elastic and swelling anisotropies by local control of the orientation of cellulose fibrils within the hydrogel composite. During printing, these fibrils undergo shear-induced alignment[23] as the ink flows through the deposition nozzle[24], which leads to printed filaments with anisotropic stiffness, and, hence, swelling behaviour in the longitudinal direction (along the filament length, as defined by the printing path) compared to the transverse direction (Fig. 1a). Significant cellulose fibril alignment is directly observed in the printed samples compared to isotropic cast sheets of the same material (Fig. 1b–d). Fourier analysis quantifies the relative alignment between cast and printed specimens, which indicates a clear directionality peak in the latter case (Fig. 1e and Supplementary Fig. 4). Thus, the printed architectures exhibit a fourfold difference in longitudinal and transverse swelling strains of $\alpha_{\parallel} \sim 10\%$ and $\alpha_{\perp} \sim 40\%$, respectively (Fig. 1f,g). Likewise, this signature of anisotropy is present in the elastic moduli, with longitudinal and transverse values of $E_{\parallel} \sim 40$ kPa and $E_{\perp} \sim 20$ kPa, respectively (Supplementary Figs 5 and 6). The extent of shear-induced alignment, and, hence, the magnitude of the anisotropic swelling, depends on the nozzle diameter and printing speed. For a fixed printing speed, the shear forces that align the cellulose fibrils scale inversely with nozzle size, as reflected in the observed longitudinal and transverse swelling strains (Fig. 1f).

Harnessing anisotropic swelling allows precise control over the curvature in bilayer structures[9,25]. Quantifying this requires a mathematical model for the mechanics of anisotropic plates and shells, which combines aspects of the classical Timoshenko model for thermal expansion in bilayers[26] with a tailored metric-driven approach[9,25] that employs anisotropic swelling to control the embedding of a complex surface. In a bilayer system, differential swelling between the top and bottom layers induces curvature, because the layers are forced to remain in contact along the entire midplane. Thereby, the displacements, integrated from the swelling

[1]John A. Paulson School of Engineering and Applied Sciences, Harvard University, 29 Oxford Street, Cambridge, Massachusetts 02138, USA. [2]Wyss Institute for Biologically Inspired Engineering, Harvard University, 60 Oxford Street, Cambridge, Massachusetts 02138, USA. [3]School of Chemical Sciences, University of Illinois Urbana-Champaign, Urbana, Illinois 61801, USA. [4]Departments of Physics and Organismic and Evolutionary Biology, and Kavli Institute for NanoBio Science and Technology, Harvard University, 29 Oxford Street, Cambridge, Massachusetts 02138, USA. †These authors contributed equally to this work. *e-mail: lm@seas.harvard.edu; jalewis@seas.harvard.edu

© 2016 Macmillan Publishers Limited. All rights reserved

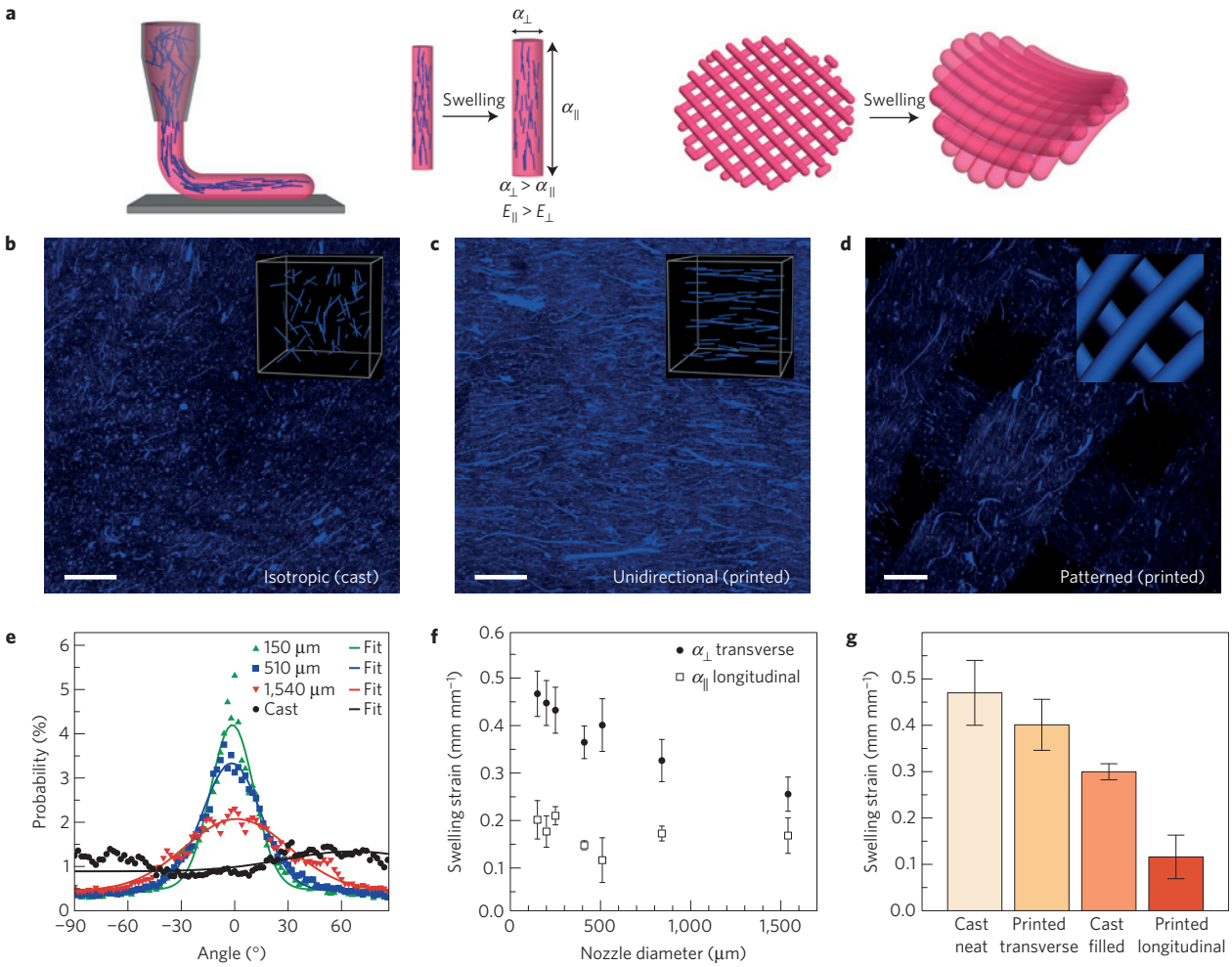

Figure 1 | Programming localized anisotropy via biomimetic 4D printing. One-step alignment of cellulose fibrils during hydrogel composite ink printing. **a**, Schematic of the shear-induced alignment of cellulose fibrils during direct ink writing and subsequent effects on anisotropic stiffness E and swelling strain α. **b**–**d**, Direct imaging of cellulose fibrils (stained blue) in isotropic (cast) (**b**), unidirectional (printed) (**c**) and patterned (printed) (**d**) samples (scale bar, 200 µm). **e**, Applying Fourier analysis to NFC-stained images allows quantification of directionality: printed unidirectional samples exhibit a clear peak at 0°, corresponding to the print direction, whereas isotropic samples show no clear directional peaks. **f**, Effect of nozzle diameter on transverse and longitudinal swelling behaviour of printed hydrogel composites. **g**, Swelling strain of cast and printed samples (nozzle diameter = 510 µm). All error bars represent the standard deviation ($n = 6$).

and curvature strain tensors, and traction along the midplane must be identical. Reflecting these conditions, we consider a theoretical model for a three-dimensional structure produced by a prescribed print path, where the print path dictates the local orientation of the cellulose fibrils. The bottom layer is printed parallel to the $\mathbf{e}_x$ direction, and the top layer has been rotated anticlockwise by θ degrees (see Supplementary Fig. 1).

The resulting curvatures depend on the elastic moduli, the swelling ratios, the ratio of layer thicknesses $m = a_{\text{bottom}}/a_{\text{top}}$ and total bilayer thickness $h = a_{\text{top}} + a_{\text{bottom}}$. The mean and Gaussian curvatures scale, respectively, as

$$H = c_1 \frac{\alpha_\parallel - \alpha_\perp}{h} \frac{\sin^2(\theta)}{c_2 - c_3\cos(2\theta) + m^4\cos(4\theta)}$$

and

$$K = -c_4 \frac{(\alpha_\parallel - \alpha_\perp)^2}{h^2} \frac{\sin^2(\theta)}{c_5 - c_6\cos(2\theta) + m^4\cos(4\theta)}$$

where the c_i are functions of the elastic constants (which are given by their equilibrium swollen values) and m (see Supplementary Information for further details). In the limit that $\theta \to 0°$, we recover the classical Timoshenko equation[26], whereas perpendicular layers ($\theta = 90°$) return a saddle-shaped structure[9].

A series of simple printed bilayer architectures allows us to explore these relationships and the quantitative connection between swelling as well as elastic anisotropy and the curvature of the target surface (Fig. 2). We first demonstrate independent control over both the mean and Gaussian curvatures, the two invariants associated with the curvature of any surface.

Positive Gaussian curvature can be generated by swelling a structure that is primarily made of concentric circles[27] (Fig. 2a). This structure is conical ($K \sim 0$) far away from the tip, but has Gaussian curvature $K \sim \epsilon^2/h^2$ concentrated near the apex, where $\epsilon \sim (\alpha_\parallel - \alpha_\perp)$. The conical opening angle, both measured and calculated using our theory, is $\theta = 52°$ (see Supplementary Information). On the other hand, almost uniform negative Gaussian curvature associated with saddle-like shapes comes from an orthogonal bilayer lattice[9] (Fig. 2b). The orthogonal swelling of each layer yields a surface that is curved oppositely along two directions—that is, a saddle-shaped surface with mean curvature $H \sim 0$ and Gaussian curvature $K \sim -\epsilon^2/h^2$. Combining these two morphologies produces a sample with zones of both positive and negative Gaussian curvature (Fig. 2c). Simple structures that

© 2016 Macmillan Publishers Limited. All rights reserved

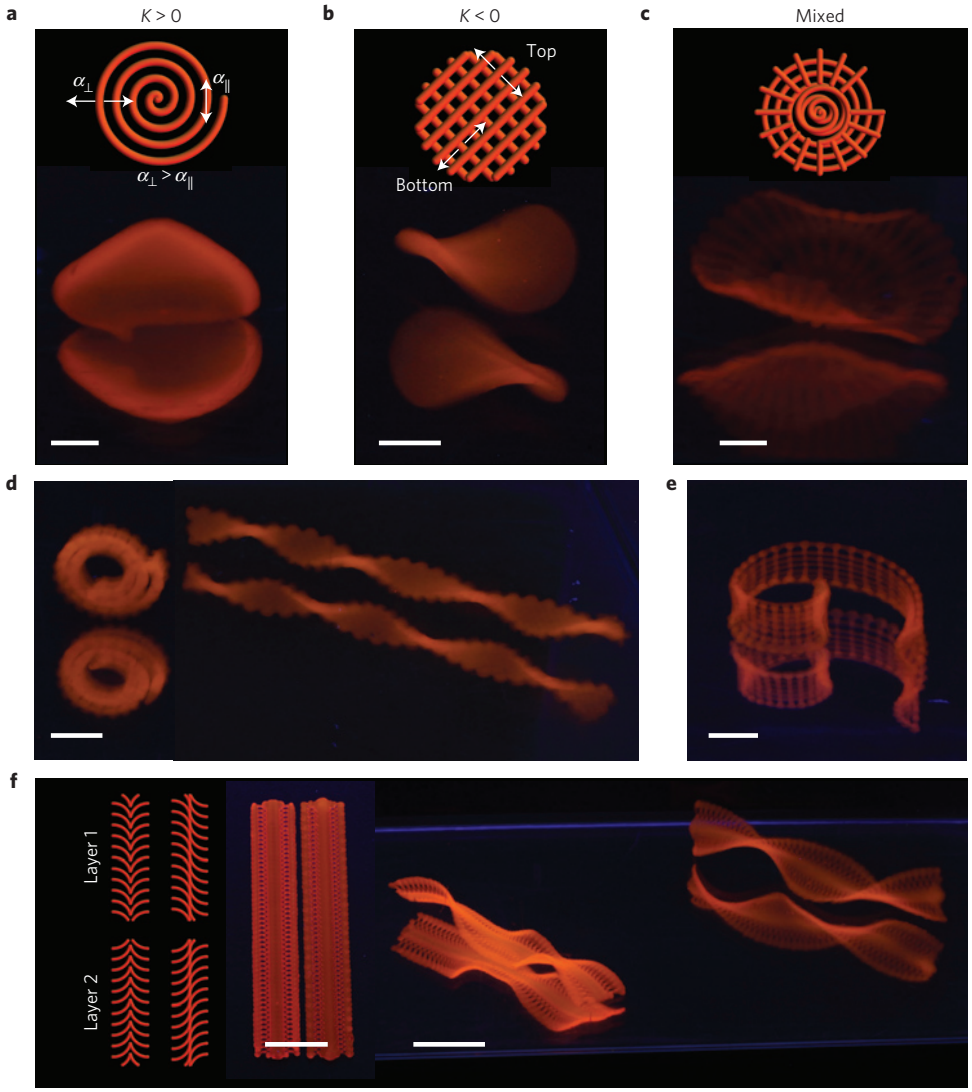

Figure 2 | Printing simple architectures with precise control over mean and Gaussian curvatures. a–c, Print paths and final swollen geometries display positive (**a**), negative (**b**) and varying Gaussian curvature (**c**) (scale bar, 2.5 mm). **d**, Bending and twisting conformations are possible with strips of 90°/0° (left) and −45°/45° (right) print path orientations (see text for details). **e**, A gradient in local interfilament spacing generates a logarithmic spiral (scale bars, 5 mm). **f**, Breaking lateral symmetry in print paths order takes a ruffled structure (left) to a helicoidal structure (right) (scale bar, 10 mm).

exhibit uniform cylindrical curvature ($H \neq 0, K = 0$) arise with 90°/0° orientation of ink paths, whereas −45°/45° yields twisted bilayer strips (Fig. 2d), similar to their natural counterparts the *Erodium* awn[28] and the *Bauhinia* seed pod[9], respectively. Because interfilament spacing acts as a proxy for the thickness (see Supplementary Text), we can also make the curvature spatially inhomogeneous, leading, for example, to the logarithmic spiral (Fig. 2e and more examples in Supplementary Figs 7 and 8). Overlapping circular arcs generate a structure, which transitions from primarily swelling perpendicular to the spine of the petal to parallel to the border, leading to a surface with varying K (Fig. 2f). This structure possesses negative Gaussian curvature, which increases towards the edge. Similarly, in the print path of a ribbon, breaking translational symmetry across the midplane and replacing it by reflection symmetry yields a ruffled structure, whereas breaking the reflection symmetry across the midplane and the midline yields a helicoid[29,30] (Fig. 2f and Supplementary Movie 1). Figure 2 also illustrates our ability to control curvatures of both solid (infilled) structures and lattice-based structures with varying porosity (see Supplementary Text for details).

By combining patterns that generate simple curved surfaces, we created a series of functional folding flower architectures to demonstrate the capabilities of bio-4DP (Fig. 3). Inspired by flower opening/closing[31], we printed petals in a floral form (Fig. 3a) comprised of a bilayer lattice with a 90°/0° configuration, similar to previous bilayer strips[9,16] and see that the structure closes as it swells (see Supplementary Movie 2). As a control, we also printed an identical pattern using an ink devoid of microfibrils, and observe that it remains flat on swelling (Supplementary Fig. 9). When the petals are printed with the ink filaments oriented at −45°/45° (Fig. 3b) the resulting structure yields a twisted configuration (see Supplementary Movie 3)[9]; the chirality of the resulting structures is due to broken top–bottom symmetry of the bilayer and thence differential swelling across the thickness. Importantly, these constructs contain spanning filaments that are readily fabricated by direct writing of the viscoelastic composite ink. The interfilament spacing promotes rapid uptake of water through the filament radius (∼100 μm), leading to shape transformations that occur on the order of minutes (Fig. 3a,b), consistent with diffusion-limited dynamics (Supplementary Fig. 10). Whereas the shape transformation shown in Fig. 3 is not reversible, replacing

© 2016 Macmillan Publishers Limited. All rights reserved

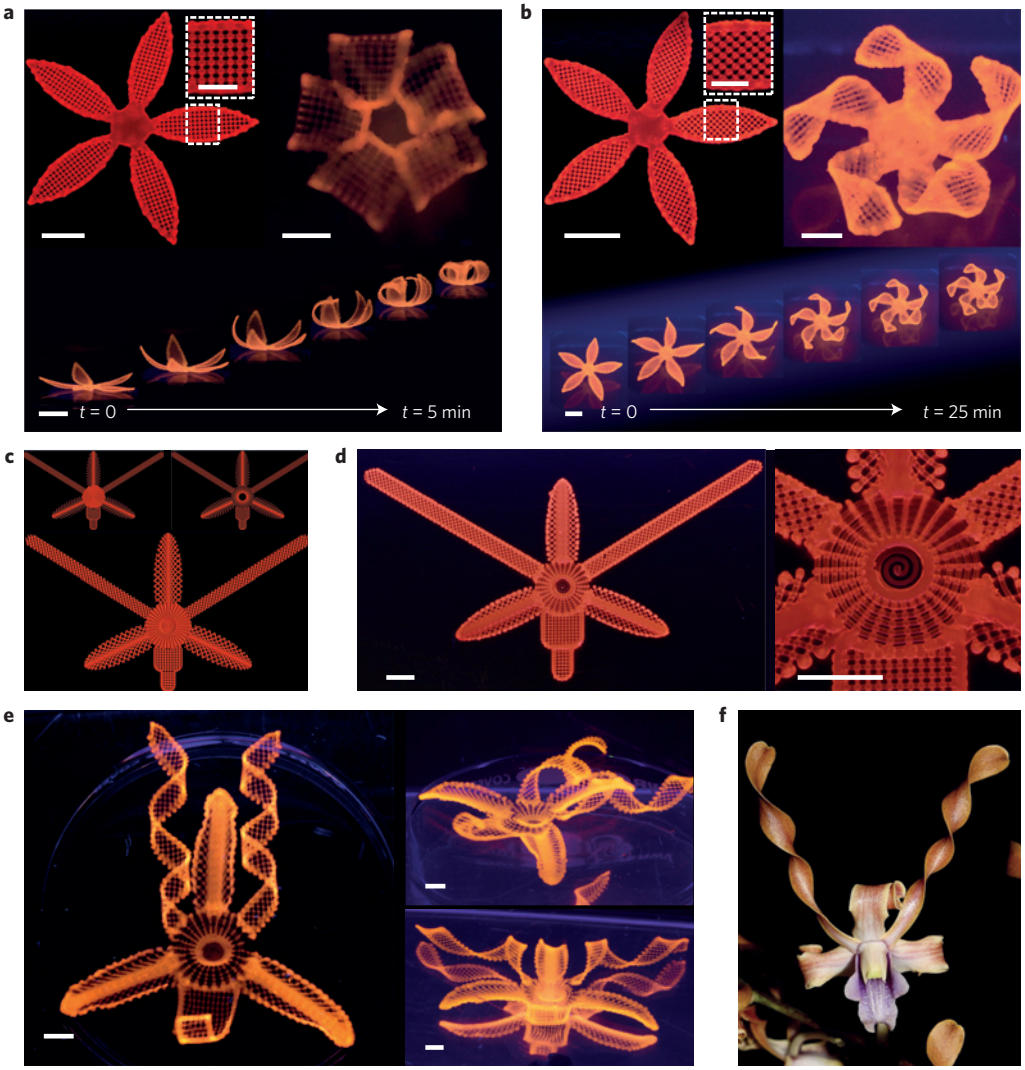

Figure 3 | Complex flower morphologies generated by biomimetic 4D printing. a,**b**, Simple flowers composed of 90°/0° (**a**) and −45°/45° (**b**) bilayers oriented with respect to the long axis of each petal, with time-lapse sequences of the flowers during the swelling process (bottom panel) (scale bars, 5 mm, inset = 2.5 mm). **c**–**f**, Print path (**c**), printed structure (**d**) and resulting swollen structure (**e**) of a flower demonstrating a range of morphologies inspired by a native orchid, the *Dendrobium helix* (courtesy of Ricardo Valentin) (**f**). Based on the print path, this orchid architecture exhibits four different configurations: bending, twisting and ruffling corolla surrounding the central funnel-like domain (scale bars, 5 mm).

the poly(*N*,*N*-dimethylacrylamide) matrix with stimuli-responsive poly(*N*-isopropylacrylamide) allows reversible shape changes in water of varying temperature (Supplementary Fig. 11 and Supplementary Movie 4).

As an example of the versatility of bio-4DP, we mimic the complexity of the orchid *Dendrobium helix* by encoding multiple shape-changing domains. The print path is designed with discrete bilayer orientations in each petal (Fig. 3c,d, see Supplementary Movie 5 for a video of the printing process, and Supplementary Fig. 12 for the fibril alignment needed for these complex shapes). The resulting 3D morphology (Fig. 3e and Supplementary Movie 6) following swelling in water resembles the orchid (Fig. 3f) and exhibits four distinct types of shape change (three different petal types and the flower centre), based on configurations demonstrated in Figs 2 and 3a,b.

In each of the previous examples, our model can be used to predict the final curvature based on the print path, which naturally suggests the inverse problem: how may we design print paths associated with specific target surfaces? In an illustrative demonstration, we harness continuous, detailed control over print path, predicted by our model and enabled by bio-4DP, to mimic the complex curvature of the calla lily flower (*Zantedeschia aethiopica*, Fig. 4a). Our model enables the translation of a complex three-dimensional surface (Fig. 4b and Supplementary Text) into the two-layered print path (Fig. 4d and Supplementary Movie 7) required to achieve this shape using only the local curvatures (Fig. 4c), swelling ratio, elastic constants, height and size of the structure. Gauss's Theorema Egregium dictates the metric of one of the layers (as demonstrated in ref. 25) whereas our mechanical model determines the architecture of the other layer. The good agreement between the final 3D shape, calculated theoretically (Fig. 4e) and printed experimentally (Fig. 4f), illustrates our unprecedented control over smooth gradients in curvature and the consequent ability to create shapes that are almost impossible to create by any other method. In addition, our bio-4DP approach allows the fabrication of shape changing elements beyond planar bilayers, by encoding anisotropy in the *z*-direction (Supplementary Fig. 13).

Our 4D printing method relies on a combination of materials and geometry that can be controlled in space and time. This technique has potential as a platform technology, where the hydrogel composite ink design can be extended to a broad

© 2016 Macmillan Publishers Limited. All rights reserved

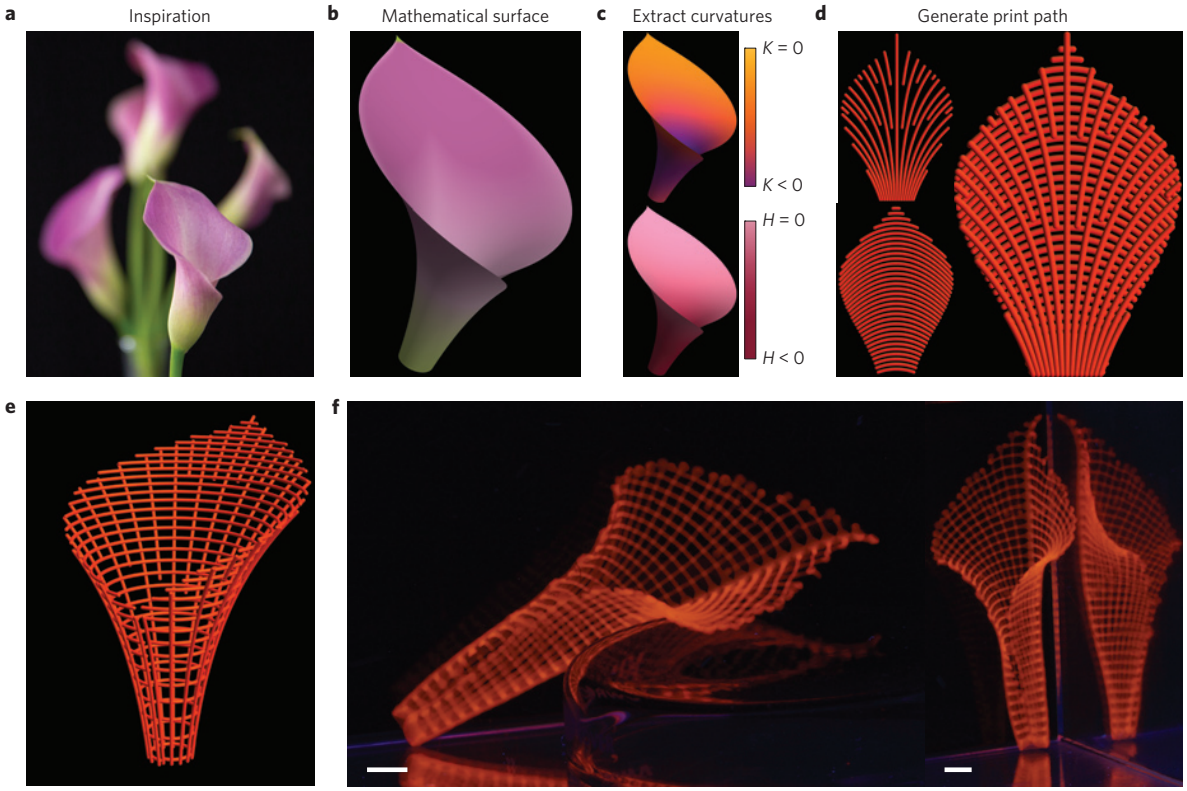

Figure 4 | Predictive 4D printing of biomimetic architectures. a–d, A native calla lily flower (**a**) inspires the mathematically generated model of the flower (**b**), with a well-defined curvature (**c**), that leads to the print path (**d**) obtained from the curvature model to create the geometry of the flower on swelling (see text and Supplementary Information). **e**,**f**, After swelling, the transformed calla lily (**f**) exhibits the same gradients of curvature as the predicted model (**e**), nozzle size = 410 μm (scale bars, 5 mm).

range of matrices (for example, liquid-crystal elastomers) and anisotropic fillers (for example, metallic nanorods) that when combined with flow-induced anisotropy allows us to produce dynamically reconfigurable materials with tunable functionality. Through the control of printing parameters, such as filament size, orientation, and interfilament spacing, we can create mesoscale bilayer architectures with programmable anisotropy that morph into given target shapes, predicted by our model, on immersion in water. All together, owing to our biocompatible and flexible ink design, our study opens new avenues for creating designer shape-shifting architectures for tissue engineering, biomedical devices, soft robotics and beyond.

Methods

Methods and any associated references are available in the online version of the paper.

Received 13 November 2015; accepted 17 December 2015; published online 25 January 2016

References

1. Hu, J., Meng, H., Li, G. & Ibekwe, S. I. A review of stimuli-responsive polymers for smart textile applications. *Smart Mater. Struct.* **21,** 053001 (2012).
2. Felton, S., Tolley, M., Demaine, E., Rus, D. & Wood, R. A method for building self-folding machines. *Science* **345,** 644–646 (2014).
3. Randall, C. L., Gultepe, E. & Gracias, D. H. Self-folding devices and materials for biomedical applications. *Trends Biotechnol.* **30,** 138–146 (2012).
4. Fernandes, R. & Gracias, D. H. Self-folding polymeric containers for encapsulation and delivery of drugs. *Adv. Drug Deliv. Rev.* **64,** 1579–1589 (2012).
5. Kuribayashi-Shigetomi, K., Onoe, H. & Takeuchi, S. Cell origami: self-folding of three-dimensional cell-laden microstructures driven by cell traction force. *PLoS ONE* **7,** e51085 (2012).
6. Forterre, Y., Skotheim, J., Dumais, J. & Mahadevan, L. How the Venus flytrap snaps. *Nature* **433,** 421–425 (2005).
7. Awell, B. J., Kriedemann, P. E. & Turnbull, C. G. N. *Plants in Action* (Macmillan Education AU, 1999).
8. Reyssat, E. & Mahadevan, L. Hygromorphs: from pine cones to biomimetic bilayers. *J. R. Soc. Interface* **6,** 951–957 (2009).
9. Armon, S., Efrati, E., Kupferman, R. & Sharon, E. Geometry and mechanics in the opening of chiral seed pods. *Science* **333,** 1726–1730 (2011).
10. Fratzl, P. & Burgert, I. Actuation systems in plants as prototypes for bioinspired devices. *Phil. Trans. R. Soc. A* **6,** 1541–1557 (2009).
11. Ge, Q., Qi, H. J. & Dunn, M. L. Active materials by four-dimension printing. *Appl. Phys. Lett.* **103,** 131901 (2013).
12. Ratna, D. & Karger-Kocsis, J. Recent advances in shape memory polymers and composites: a review. *J. Mater. Sci.* **43,** 254–260 (2008).
13. Erb, R. M., Sander, J. S., Grisch, R. & Studart, A. E. R. Self-shaping composites with programmable bioinspired microstructures. *Nature Commun.* **4,** 1712 (2012).
14. Thérien-Aubin, H., Wu, Z. L., Nie, Z. & Kumacheva, E. Multiple shape transformations of composite hydrogel sheets. *J. Am. Chem. Soc.* **125,** 4834–4839 (2013).
15. Tibbits, S. 4D printing: multi-material shape change. *Archit. Des.* **84,** 116–121 (2014).
16. Ionov, L. Bioinspired microorigami by self-folding polymer films. *Macromol. Chem. Phys.* **214,** 1178–1183 (2012).
17. Na, J. H. *et al*. Programming reversibly self-folding origami with micropatterned photo-crosslinkable polymer trilayers. *Adv. Mat.* **27,** 79–85 (2015).
18. Liu, Y., Boyles, J. K., Genzer, J. & Dickey, M. D. Self-folding of polymer sheets using local light absorption. *Soft Matter* **8,** 1764–1769 (2012).
19. Lewis, J. A. Direct ink writing of 3D functional materials. *Adv. Funct. Mater.* **16,** 2193–2204 (2006).
20. Oytun, F., Kahveci, M. U. & Yagci, Y. Sugar overcomes oxygen inhibition in photoinitiated free radical polymerization. *J. Polym. Sci. A* **51,** 1685–1689 (2013).
21. Josset, S. *et al*. Energy consumption of the nanofibrillation of bleached pulp, wheat straw and recycled newspaper through a grinding process. *Nord. Pulp Paper Res. J.* **29,** 167–175 (2014).

© 2016 Macmillan Publishers Limited. All rights reserved

22. Haraguchi, K. & Takehisa, T. Nanocomposite hydrogels: a unique organic-inorganic network structure with extraordinary mechanical, optical, and swelling/de-swelling properties. *Adv. Mater.* **14,** 1120–1124 (2002).
23. Compton, B. G. & Lewis, J. A. 3D-printing of lightweight cellular composites. *Adv. Mater.* **26,** 5930–5935 (2014).
24. Smay, J. E., Cesarano, J. & Lewis, J. A. Colloidal inks for directed assembly of 3-D periodic structures. *Langmuir* **18,** 5429–5437 (2002).
25. Aharoni, H., Sharon, E. & Kupferman, R. Geometry of thin nematic elastomer sheets. *Phys. Rev. Lett.* **113,** 257801 (2014).
26. Timoshenko, S. Analysis of bi-metal thermostats. *J. Opt. Soc. Am.* **11,** 233–255 (1925).
27. Modes, C. D., Bhattacharya, K. & Warner, M. Gaussian curvature from flat elastic sheets. *Proc. R. Soc. A* **467,** 1121–1140 (2011).
28. Abraham, Y. *et al*. Titled cellulose arrangement as a novel mechanism for hygroscopic coiling in the stork's bill awn. *J. R. Soc. Interface* **9,** 640–647 (2012).
29. Liang, H. & Mahadevan, L. The shape of a long leaf. *Proc. Natl Acad. Sci. USA* **106,** 22049–22054 (2009).
30. Liang, H. & Mahadevan, L. Growth, geometry, and mechanics of a blooming lily. *Proc. Natl Acad. Sci. USA* **108,** 5516–5521 (2011).
31. van Doorn, W. G. Flower opening and closure: a review. *J. Exp. Bot.* **54,** 1801–1812 (2003).

Acknowledgements

A.S.G. and J.A.L. were supported by the Army Research Office Award No. W911NF-13-0489. E.A.M. and L.M. were supported by the NSF DMR 14-20570, Materials Research Science and Engineering Center, MRSEC and NSF DMREF 15-33985. We thank D. Stepp (ARO), A. Balazs (U. Pittsburgh), M. Brenner (Harvard) and B. Compton for useful discussions. We thank T. Zimmermann and the researchers at the Applied Wood Materials Laboratory at EMPA for providing samples of nanofibrillated cellulose. We also thank D. Kolesky for assistance with confocal imaging, D. Fitzgerald and J. Minardi for help with initial G-code programming, R. Valentin for permission to print a copy of his orchid photograph, and L. K. Sanders for help with photography and videography.

Author contributions

A.S.G., R.G.N. and J.A.L. developed the 4D printing concept. A.S.G. designed the ink composition, printed and prepared all samples, obtained photographic images, and characterized alignment, swelling, mechanical and rheological properties. E.A.M. and L.M. developed the theoretical model. E.A.M. rendered and calculated the desired shapes and print paths, and generated the G-code for printing. A.S.G., E.A.M., L.M. and J.A.L. wrote the manuscript. A.S.G. and E.A.M. developed the figures. All authors commented on the manuscript.

Additional information

Supplementary information is available in the online version of the paper. Reprints and permissions information is available online at www.nature.com/reprints. Correspondence and requests for materials should be addressed to L.M. or J.A.L.

Competing financial interests

The authors declare no competing financial interests.

© 2016 Macmillan Publishers Limited. All rights reserved

Methods

The general procedure for creating 4D printed architectures involves the preparation of ink containing clay, monomer, NFC, photoinitiator, enzyme/glucose and deionized water. Architectures are printed at room temperature in air, and ultraviolet cured after print completion. Samples are immersed in deionized water to allow swelling and shape transformation.

Ink preparation and details. Synthetic hectorite clay, Laponite XLG (Southern Clay Products), is added, enabling polymerization to initiate from the surface on the clay due to the high cationic exchange capacity of the clay[32]. The clay forms a strong physical, multifunctional crosslinker, with recent modelling suggesting that an increase in clay content results in an increase in inter-particle crosslinking polymer chains[33]. The network gel formed by the process imparts high stretchability and strength compared to covalently crosslinked hydrogels without clay[22]. As higher clay concentrations result in higher crosslink densities, and lower swelling, we sought a minimal clay concentration. Thus, ~10 wt% clay was chosen as the minimum clay concentration needed for printed filaments to flow and retain shape as desired. Our source for nanofibrillated cellulose (NFC) is unbleached and processed directly from soft wood pulp (*Picea abies* and *Pinus* spp.), graciously donated by the Applied Wood Material Lab at EMPA. The maximum NFC concentration that allowed for smooth, clog-free print behaviour was ~0.8 wt%, and thus was chosen for all experiments. The monomer used in this gel is *N*,*N*-dimethylacrylamide or *N*-isopropylacrylamide, which forms a biocompatible hydrogel capable of significant swelling in water, both of which have been shown to utilize the aforementioned clay-crosslinking system[34].

Oxygen inhibition (OI) is a major limitation in 3D printing polymer inks undergoing free-radical polymerization. OI can lead to hundreds of micrometres or more of poorly cured surface gel. With 3D printed features of this same scale, it is a major hurdle to overcome. To prevent OI we report the use of a naturally occurring oxygen-scavenging enzyme, glucose oxidase, which has recently been demonstrated to improve ambient ultraviolet polymerization in aqueous hydrogels[20]. We report the use of glucose oxidase/glucose for the first time in 3D printed hydrogel inks, an essential addition for successful polymerization in ambient conditions; without the enzyme, 200 μm printed features are unable to be cured in ambient conditions, whereas the addition of the glucose oxidase enables cured architectures with no detectable OI.

NFC is diluted from a stock solution to deoxygenated water under nitrogen flow, and mixed thoroughly using a Thinky mixer (ARE-310, Thinky) in a closed container. Laponite XLG clay is then added under nitrogen flow and mixed again using the Thinky mixer. Monomer, *N*,*N*-dimethylacrylamide (DMAm) or *N*-isopropylacrylamide (NIPAm) (Sigma Aldrich, unmodified), is added to this NFC-clay solution under nitrogen flow and mixed again using the Thinky mixer. Irgacure 2959 (BASF) is added as the ultraviolet photoinitiator. D-(+)-glucose (Sigma Aldrich) and glucose oxidase (from Aspergillus niger, Sigma Aldrich) are added as oxygen scavengers. Under nitrogen flow the ink is hand mixed, followed by mixing using the Thinky mixer. The final concentrations of each component are as follows: 77.6% deionized water, 0.73% NFC, 9.7% Laponite XLG clay, 7.8% monomer, 0.097% Irgacure 2959, 0.23% glucose oxidase, 3.8% glucose. Finally 1 vol% of a 5 mg ml^{-1} solution of a monomeric rhodamine dye (PolyFluor 570-methacryloxyethyl thiocarbonyl rhodamine B, Polysciences) is added under nitrogen flow and mixed using the Thinky mixer. Under nitrogen flow the ink is loaded into a syringe barrel and centrifuged to remove bubbles. The ink is then mounted to the printer and attached to a controlled air pressure input (Nordson EFD). Via Luer-lock connection a variety of commercial nozzles of varying diameter (Nordson EFD) can be attached. All nozzles were stainless steel, straight tips, with 10 mm nozzle lengths.

Printing procedure. Print paths were generated via production of G-code which outputs the XYZ motion of the 3D printer (ABG 10000, Aerotech). G-code was generated either by hand, using MeCode Python scripting (Jack Minardi (Voxel8), Daniel Fitzgerald (WPI)), or by scripting in Mathematica. Samples were printed on glass slides covered with a Teflon adhesive film (Bytac, Saint-Gobain) and cured for 200 s using an Omnicure ultraviolet source (Series 2000, Lumen Dynamics). After curing, the printed architecture is coated in a thin film of DI water to remove it from the substrate. The sample was then immersed in DI water to allow swelling and shape change.

Characterizing alignment and swelling. To test NFC alignment we printed unidirectional, solid-infilled samples with various sizes of nozzles (150–1,500 μm diameter). We also fabricated NFC filled and unfilled cast hydrogel samples for comparison. Longitudinal (print direction) and transverse strains were calculated by measuring sample dimensions as fabricated and after reaching equilibrium swelling in DI water, or approximately five days. These samples were then stained via immersion in 5 ml of a 0.1 mg ml^{-1} solution of Calcofluor White (Sigma Aldrich), with 200 μl of 10 wt% potassium hydroxide solution added, for 24 h. They were removed from the staining solution and soaked in DI water for 24 h, and then imaged via confocal microscopy (LSM710, Zeiss). Z slices of approximately 10 μm were acquired and stacked into maximum projection images using ImageJ. To quantify alignment, the ImageJ plugin Directionality (creator: J. Yvez-Tinevez), was applied to the unmodified maximum projection images, resulting in a histogram of relative alignment in different orientations. A Gaussian fit is applied to the resulting histograms.

Mechanical testing. Tensile specimens were prepared via printing and curing. The print path of transverse and longitudinal orientations are shown in Supplementary Fig. 5. Samples were tested either immediately after fabrication or after soaking in DI water for five days. The samples were tested on an Instron mechanical testing machine (Model 3342) with a 10 N load cell at a rate of 100 mm min^{-1} until failure. Stress and strain were calculated via initial specimen dimensions. Moduli were calculated from linear regions of the stress–strain curves.

Rheological characterization. Inks rheology was characterized via testing on a rheometer (DHR-3, TA Instruments) with a 40 mm diameter, 2.005° cone-plate geometry. Flow experiments were conducted via a logarithmic sweep of shear rates (0.1–10,001 s^{-1}). Oscillation experiments were conducted via a fixed frequency of 1 Hz and oscillatory strain of 0.01, with a sweep of stress (0.1–3,000 Pa). All experiments were performed in ambient conditions with a gap height of 56 μm and preliminary soak time of 60 s.

Macro imaging. All photographic images were taken under a broad spectrum ultraviolet light source to excite the rhodamine dye in the ink. Images were taken with DSLR cameras (Mark III or Rebel T3i, Canon) with a variety of lenses. As-printed specimens were photographed in ambient conditions, while resulting shape transformations were captured in an acrylic enclosure containing deionized water.

Code availability. G-code (print path) for all structures printed in Figs 2–4 is available on request.

References

32. Haraguchi, K., Li, H.-J., Matsuda, K., Takehisa, T. & Elliott, E. Mechanism of forming organic/inorganic network structures during *in-situ* free-radical polymerization in PNIPA-clay nanocomposite hydrogels. *Macromolecules* **38,** 3482–3490 (2005).
33. Yong, X., Kuksenok, O. & Balazs, A. C. Modeling free radical polymerization using dissipative particle dynamics. *Polymer* **72,** 217–225 (2015).
34. Haraguchi, K., Murata, K. & Takehisa, T. Stimuli-responsive nanocomposite gels and soft nanocomposites consisting of inorganic clays and copolymers with different chemical affinities. *Macromolecules* **45,** 385–391 (2012).

© 2016 Macmillan Publishers Limited. All rights reserved